ACS OMEGA

http://pubs.acs.org/journal/acsodf

Article

Temperature- and Defect-Induced Uniaxial Tensile Mechanical Behaviors and the Fracture Mechanism of Two-Dimensional Silicon Germanide

A. S. M. Jannatul Islam, Md. Shahadat Akbar, Md. Sherajul Islam,* and Jeongwon Park

Cite This: *ACS Omega* 2021, 6, 21861−21871

Read Online

ACCESS | Metrics & More | Article Recommendations | Supporting Information

ABSTRACT: Recently, monolayer silicon germanide (SiGe), a newly explored buckled honeycomb configuration of silicon and germanium, is predicted to be a promising nanomaterial for next-generation nano-electromechanical systems (NEMS) due to its intriguing electronic, optical, and piezoelectric properties. In the NEMS applications, the structure is subjected to uniaxial tensile mechanical loading, and the investigation of the mechanical behaviors is of fundamental importance to ensure structural stability. Here, we systematically explored the uniaxial tensile mechanical properties of 2D-SiGe through molecular dynamics simulations. The effects of temperature ranges from 300 to 1000 K and vacancy defects, for instance, point and bi vacancy, for both armchair and zigzag orientations of 2D-SiGe were investigated. In addition, the influence of system areas and strain rates on the stress−strain performance of 2D-SiGe has also been studied. With the increase in temperature and vacancy concentration, the mechanical properties of 2D-SiGe show decreasing behavior for both orientations and the armchair chirality shows superior mechanical strength to the zigzag direction due to its bonding characteristics. A phase transformation-induced second linearly elastic region was observed at large deformation strain, leading to an anomalous stress−strain behavior in the zigzag direction. At 300 K temperature, we obtained a fracture stress of ∼94.83 GPa and an elastic modulus of ∼388.7 GPa along the armchair direction, which are about ∼3.17 and ∼2.83% higher than the zigzag-oriented fracture strength and elastic modulus. Moreover, because of the strong regularity interruption effect, the point vacancy shows the largest decrease in fracture strength, elastic modulus, and fracture strain compared to the bi vacancy defects for both armchair and zigzag orientations. Area and strain rate investigations reveal that 2D-SiGe is less susceptible to the system area and strain rate. These findings provide a deep insight into controlling the tensile mechanical behavior of 2D-SiGe for its applications in next-generation NEMS and nanodevices.

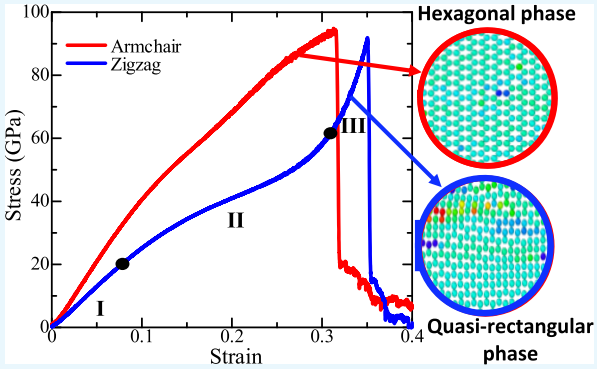

INTRODUCTION

With the advent of nanotechnology, the demand for nano-electromechanical systems (NEMS), including nanoresonators, nanocomposites, nanoenergy-harvesting systems, and conversion systems, has increased considerably to mitigate the shortcoming of microscale systems.[1,2] However, the mechanical failure problem of the present NEMS is a great concern.[3,4] Nanoscale materials with ultrahigh tensile strength and superior electronic properties are thus highly demanded to realize the next-generation NEMS and nanoelectronics. The unique electronic properties,[5,6] enormous surface-to-volume ratio, and excellent mechanical properties of two-dimensional (2D) materials make them favorable for NEMS fabrication.[7] Although the first exfoliated 2D material, graphene,[8] receives considerable interest for NEMS fabrication, its zero bandgap feature makes it unlikely in nanoelectronics and NEMS applications.[9] Moreover, another limitation of graphene application in nanoelectronics is the difficulty of integration into the current Si-based technology.[10] Beyond graphene, the group IV-based diatomic structures, including sp^2 hybridized planar silicon carbide (SiC)[11] and sp^2−sp^3 hybridized low-buckled silicon germanide (SiGe),[10,11] have drawn strong attention in the applications of NEMS and nanodevices due to their intriguing properties. Specifically, monolayer SiGe possesses a bandgap of ∼0.285 eV[10,12] and endorses a very insignificant variation in the electronegativity of silicon and germanium atoms,[11,13] making it the research focus recently. Monolayer SiGe is very much well-matched with existing silicon-based electronics, and hence, the progress in the

Received: March 29, 2021
Accepted: August 4, 2021
Published: August 17, 2021

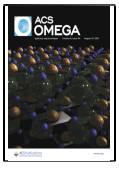

© 2021 The Authors. Published by American Chemical Society

synthesis of SiGe is exciting and has shown excessive attention in the present NEMS and nanoelectronics.[12] Moreover, monolayer SiGe is found to be energetically favorable compared to other group IV elemental systems.[13,14] Due to the buckled geometry, SiGe shares most of the significant electronic characters of graphene, for example, Dirac cone behavior, high carrier mobility, and Fermi velocity with certain unique advantages comprising better tunability of the bandgap, substantial spin-orbit coupling, and easier valley polarization, which are very imperative for electronics, valleytronics, and spintronics.[12,13,15] Moreover, monolayer SiGe is also expected to be very suitable for anode materials in Li and Na-ion batteries.[16]

However, to better design the NEMS using 2D-SiGe, investigation of the mechanical behavior is crucial both from a technical perspective for its unfailing uses and from a central significance in realizing its deformation physics. Along with superior mechanical behavior, the extraordinary electronic bandgap is also essential for SiGe to be suitable for NEMS and nanoelectronic applications, which depends significantly on the loading direction.[12] Using a trifling biaxial tensile strain that can be created through lattice constant variation with the substrate, group IV diatomic 2D systems display no important modifications in the band diagram since the biaxial strain conserves all crystal regularities.[17,18] However, it has been reported that uniaxial strain can change the electronic bandgap in the diatomic structure, especially in 2D-SiGe honeycomb lattice, whether it was compressive or tensile due to the inversion symmetry breakdown.[19,20] Therefore, rather than the biaxial strain, the uniaxial strain is very much significant for the mechanical properties of the monolayer SiGe system. Usually, the fracture strength of nanostructured materials is considerably influenced by the system temperature and chirality.[21−23] For instance, with the strengthening of system temperature, the thermal trembling properties enhance significantly. Hence, the breakdown progression may change from a brittle to a ductile manner at extreme temperature and lead to a declined fashion in the mechanical strength.[22,23] In addition, along with the loading direction and system temperature, mechanical strength significantly depends on the structural defects.

From a practical standpoint, when nanomaterials are synthesized experimentally or developed from their bulk counterpart, various structural defects, such as bi vacancy (BV), point vacancy (PV), ad-atoms defect, isotope defect, stone−thrower−wales defects (SW), etc.,[22,24−28] are generated, and they can lessen the mechanical strength of the nanomaterial considerably because of their strong symmetry breakdown effect. Lately, the impact of diverse defects on the mechanical strength of various nanosheets such as monolayer silicon carbide, MoS_2, germanene, and stanene has been explored.[22,29−32] These reports proposed that the defected sheet ruptures at a breaking strength that is substantially lesser related to the rupture strength of the perfect ones, and increasing the density of defects can considerably lessen the fracture strength, elastic modulus, and fracture strain. In recent years, several experimental and DFT-based first-principles investigations have been performed on 2D-SiGe to explore its electronic, ferromagnetic, and thermodynamic stability, topological phase transition, hydrogenation, and gas adsorption behaviors.[10,12−14,16,19,33] However, the uniaxial tensile mechanical properties and fracture phenomenon of the SiGe monolayer have not been explored yet. The influence of temperature, strain rate, and sheet area on the mechanical behavior of 2D-SiGe is unknown. Moreover, the impacts of the different defects such as PV and BV on the tensile strength are also unfamiliar.

In this work, we have carried out a rigorous and systematic investigation of the mechanical behaviors of 2D-SiGe. Classical molecular dynamics simulation considering uniaxial tensile strain is applied for the exploration of fracture strength, elastic modulus, and fracture strain for both the armchair and zigzag directions. The impacts of temperature, sheet size, and strain rate variations are investigated elaborately. The effects of two types of vacancy defects, namely, BV and PV, with a concentration ranging from 1 to 3%, are explored. In addition, the rupturing phenomenon is analyzed considering the chirality, temperature, and vacancy defects. Our findings show that armchair SiGe is more rigid than zigzag SiGe, and with the increase in temperature, the ultimate fracture strength, strain, and elastic modulus show a linearly decreasing trend for both armchair and zigzag directions. The sheet size and strain rate show little variation in the calculated mechanical properties of 2D-SiGe. Moreover, for both directions, the PV defects show a more significant reduction of tensile mechanical properties than the BV defect due to its more substantial symmetry breakdown effect.

Computational Details. We employed molecular dynamics simulations via the LAMMPS package[34] to explore the tensile mechanical properties of 2D-SiGe. To describe the atomistic interactions concerning Si−Si, Ge−Ge, and Si−Ge atoms in the MD simulation, the classical Tersoff potential developed by Tersoff.[35] has been utilized. The Tersoff potential is suitable for the mechanical behavior simulation of 2D-SiGe because it successfully reproduced the 2D-SiGe physical phenomenon previously, which was in good harmony with DFT calculations.[13] Furthermore, the Tersoff potential also comprises two body and three body terms, which are very much necessary for exposing the bond breaking and bond stretching of 2D-SiGe. All the simulations were executed for three different initial conditions (i.e., molecular velocity) to perform error analysis. The resultant errors perceived from the simulation have been inserted into the results. The OVITO package was also used to visualize the crack propagation and deformation studies.[36]

We considered a 2D-SiGe nanosheet consisting of 6000 atoms with a dimension of 419.5 nm^2 (20.88 nm long and 20.09 nm wide) and buckling height of 0.58 Å as shown in Figure 1a,b.

Periodic boundary conditions were employed in all three dimensions. The thickness along the *Z*-direction was kept high

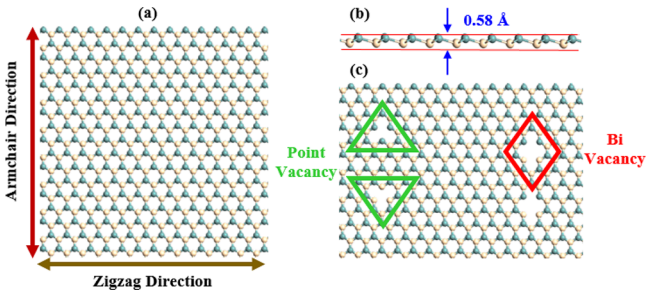

Figure 1. (a) Atomistic configuration of the considered 2D-SiGe. (b) Buckled structure of 2D-SiGe. (c) Pictorial representation of point and bi vacancy with the removal of single and double atoms of 2D-SiGe.

https://doi.org/10.1021/acsomega.1c01691
ACS Omega 2021, 6, 21861−21871

so that the atoms do not interact across the periodic boundary in the Z (out-of-plane)-direction, and only monolayer SiGe was considered in the simulation. The energy (potential) minimization of the system was performed via the conjugate gradient (CG) method. The stopping tolerance values for energy and force were considered as 10^{-8} and 10^{-8} eV/Å, respectively. The maximum iterations of the minimizer and highest force/energy evaluations were considered as 5000 and 10,000, respectively. The iterations were terminated when one of the stopping criteria is satisfied. After energy minimization, we applied equilibration simulations for 50 ps using an NVE (microcanonical) ensemble. Again, the system pressure was equilibrated at a pressure of 1 bar using an NPT (isothermal, isobaric) ensemble for 40 ps. The NPT ensemble reconfigures the system and eliminates all inner stress developed. Afterward, we applied an NVT (canonical) ensemble for 20 ps for thermal equilibration. The temperature was varied from 300 to 1000 K, and we used similar relaxation steps to achieve thermal equilibration at each temperature. In every relaxation step, we ensured proper convergence of the potential energy and desired thermodynamic quantities. In the MD simulation, we applied a time step of 1 fs for solving the equation of motion with the Velocity Verlet algorithm. Afterward, we have applied a fixed strain rate of 10^9 s^{-1} along with the deformation directions (armchair and zigzag). Although the employed strain rate is comparatively greater than the practical circumstances, this high strain rate is very much suitable in atomistic simulations to investigate the material failure phenomena with a reasonable computational resource.[22,37] The atomic stresses under uniaxial tensile deformation are explored using virial stress, which can be expressed as[38]

$$\sigma_{\text{virial}}(r) = \frac{1}{\Omega}\sum_{i}\left[\left(-m_i\dot{u}_i \otimes \dot{u}_i + \frac{1}{2}\sum_{j\neq i} r_{ij} \otimes f_{ij}\right)\right] \quad (1)$$

where the summation is considered for all the particles in the volume, m_i represents the mass of particle i, $\dot{u}_i$ represents the time derivative of the movement, r_{ij} represents the position vector, and f_{ij} represents the interatomic force employed on particle i by particle j.

RESULTS AND DISCUSSION

The stress−strain response curves at 300 K along the armchair and zigzag orientations are presented in Figure 2a. For armchair-oriented 2D-SiGe, the stress−strain behavior shows a linear correlation nearly up to the fracture strength point and finally finishes with a quick decay, ensuing in a brittle fracture of the sheet. However, for zigzag-oriented 2D-SiGe, spuriously high bond forces and nonphysical results are noticed at large deformation. The whole stress−strain relationship can be divided into three parts, i.e., part I, part II, and part III. In part I, due to the elastic response of the bonds, the stress shows a linear increasing trend with the strain up to 8%. In part II, due to the combined effect of bond angle variation and bond elongation, the stress shows a nonlinear elasticity up to a critical strain of around 32%. However, when the strain increases to more than 32%, another linear stress−strain region is initiated, regarded as the "second linearly elastic deformation (SLED)", and is indicated by part III. Previous studies reported that the cut-off distance used in the interatomic potential and phase transformation can significantly affect the mechanical behavior of zigzag-oriented 2D systems.[39−41] As

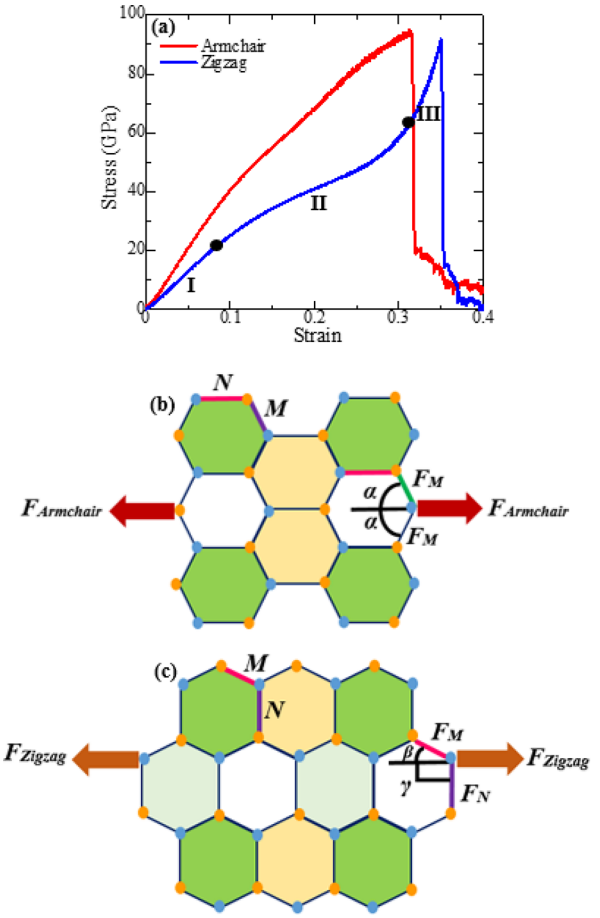

Figure 2. (a) Impact of chiral directions on the stress−strain response of 2D-SiGe. Force components along the (b) armchair and (c) zigzag orientations.

the employed Tersoff potential shows the expected results for the armchair orientation, therefore, it is anticipated that the phase transformation (which will be discussed in the later part) may cause this irregular stress−strain behavior for zigzag-oriented 2D-SiGe.[41]

Maximum tensile strengths of ∼94.83 and ∼91.92 GPa in the armchair and zigzag orientations, respectively, are obtained at 300 K. On the other hand, the critical fracture strains are recorded as ∼0.3127 and ∼0.3604 for armchair and zigzag orientations, respectively. These considerable anisotropic mechanical behaviors along the two different chiral orientations are very similar to other 2D systems.[22,42,43] The relative variation of computed stress along the armchair and zigzag directions can be explained using Figure 2b,c. In the armchair orientation, six stress-conveying bonds are contained in every unit cell, among which four bonds have a comparative angle of 60° with the armchair orientation and the other two are parallel to the armchair orientation (shown in Figure 2b). In contrast, in the zigzag orientation, there are four stress-carrying bonds in one unit cell, and these display an angle of 30° with zigzag chirality (shown in Figure 2c). Consequently, the additional two stress-carrying bonds of the armchair chirality develop higher opposition to fracture compared to zigzag chirality. Therefore, for an identical temperature, the developed fracture strength along the armchair chirality demonstrates improved performance compared to the zigzag chirality. The comparative better fracture stress of armchair-

https://doi.org/10.1021/acsomega.1c01691
ACS Omega 2021, 6, 21861−21871

oriented 2D-SiGe can also be confirmed with the conventional mechanic's concept. Under zero strain conditions, the force components along with the armchair and zigzag chirality of a 2D-SiGe sheet (revealed in Figure 2b,c) can be estimated as

For the armchair chirality

$$F_{\text{Armchair}} = F_M \cos\alpha + F_M \cos\alpha = 2F_M \cos\alpha \quad (2)$$

Also, for the zigzag chirality

$$F_{\text{Zigzag}} = F_M \cos\beta + F_N \cos\gamma \quad (3)$$

Here, $\alpha = 60°$, $\beta = 30°$, and $\gamma = 90°$.

Hence, the explored ratio of the forces is $\frac{F_{\text{Armchair}}}{F_{\text{Zigzag}}} = \frac{1.1547}{1}$, which demonstrates the improved fracture stress behavior of the armchair chirality compared to the zigzag orientation and is well consistent to other works.[42,43]

To elucidate the phase transformation effect, we have exposed the sheet deformation profile of 2D-SiGe. As shown in Figure 3a–d, the armchair structures do not show any phase

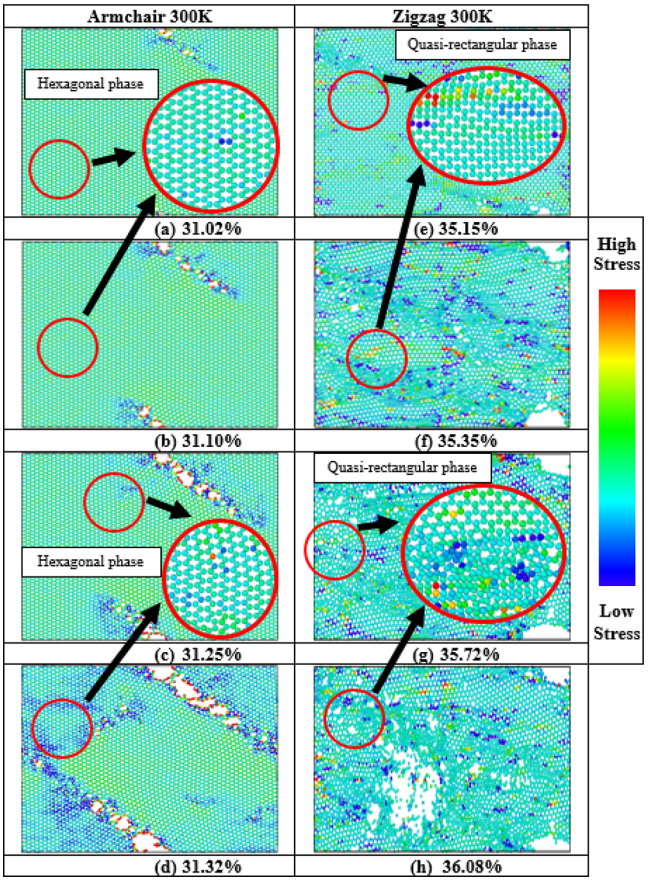

Figure 3. Tensile deformation profiles of 2D-SiGe along the (a–d) armchair and (e–h) zigzag orientations at 300 K.

variation near the fracture strain, and hexagonal lattice structure is conserved for the whole system (shown in the zoomed in insets). As a result, the SLED cannot occur in the armchair direction. However, along the zigzag direction (Figure 3e–h), the hexagonal lattice structure is no longer recognizable, and the system is converted into a quasi-rectangular lattice form due to the phase transformation (shown in the zoomed in insets). Therefore, an SLED occurs, which produces an abnormal stress–strain behavior similar to the study of zigzag-oriented graphene.[41] Due to the phase transformation, a significant amount of irregular structures is also initiated (shown in Figure 3e–h), and the fracture proceeds very quickly, responsible for the sudden damage of the zigzag-oriented 2D-SiGe. From Figure 3a–h, it is also noticed that the early damage lengthens diagonally to the pulling direction in armchair-oriented 2D-SiGe. In contrast, the expansion of the damage is nearly vertical and offers a complex destruction behavior in the zigzag-oriented sheet. These results are very analogous to 2D-C_3N.[44] With the increase in deformation strain, initiation of additional voids and the development of a single atomic string of silicon and germanium atoms are also observed in the void areas. Furthermore, the early voids are restricted to an insignificant zone. The areas near the void of the structure stay unspoiled. Similar types of deformation behaviors have also been perceived in other 2D systems, including MoS_2 and graphene.[29,45]

Nanosensors, nanoactuators, aerospace, and energy-harvesting applications demand extremely durable configurations at high temperatures.[22,37,46,47] Hence, investigation of the mechanical behavior at high temperature is extremely imperative to use the material in the next-generation NEMS and nanoelectronics. In this section, efforts are made to discover the temperature effect (300–1000 K) on the mechanical behaviors under uniaxial tensile loading. As the figures (Figure 4a,b) suggest, for both armchair and zigzag

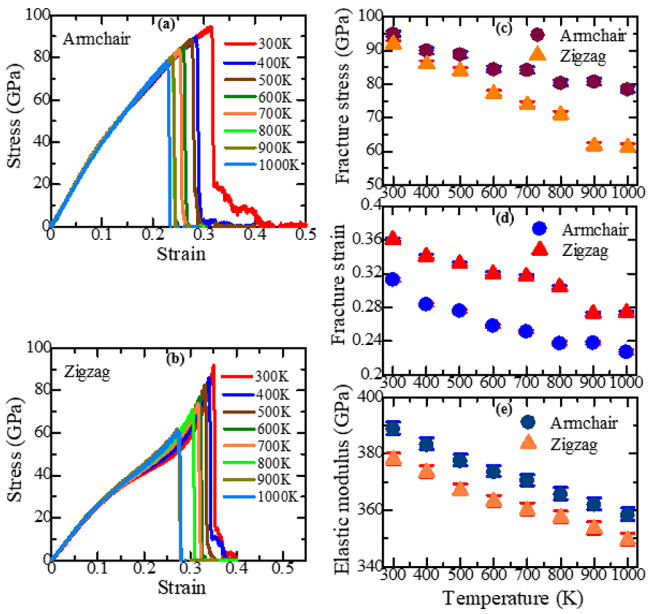

Figure 4. Impact of temperature variation on the stress–strain response of 2D-SiGe along the (a) armchair and (b) zigzag directions. Temperature-induced (c) fracture strength, (d) fracture strain, and (e) elastic modulus of 2D-SiGe along the two chiral directions.

orientations, the ultimate fracture strength shows decreasing nature when the temperature is increased. The fracture stresses drop from ~94.83 to ~78.35 GPa in the armchair orientation and from ~91.92 to ~61.22 GPa in the zigzag orientation for the temperature increases from 300 to 1000 K. The strong thermal pulsation effects of atoms at a higher temperature endorse this temperature-induced fracture strength reduction. This sturdy thermal pulsation of atoms causes the structure to be less rigid. Because of the thermal tension, the chemical

https://doi.org/10.1021/acsomega.1c01691
ACS Omega 2021, 6, 21861–21871

bonds are further expected to reach the critical bond length and consequently break. When the temperature is increased to 1000 K, the fracture strength of the pristine sheet along the zigzag orientation declines by ∼33.39%, while in the armchair orientation, the decrement is ∼17.37%. In addition, in the zigzag orientation, we found that the anomaly of the stress−strain relationship diminishes slowly, and highly brittle behavior is achieved at high temperatures. At 300 K, the fracture strains for armchair and zigzag orientations are 0.3127 and 0.3604, respectively, while those values are reduced to 0.227 and 0.2737, respectively, when the temperature is increased to 1000 K. The obtained temperature-induced tensile mechanical behavior agrees well with the results of graphene, 2D-SiC, and *h*-BCN, demonstrating that the methodology implemented here can give a reliable explanation of the mechanical properties of the present nanostructures.[22,42,43]

Next, we explore the impact of temperature on the elastic modulus of 2D-SiGe. The elastic modulus is computed by matching the stress−strain relationship to a straight line in the negligible strain zone (strain of ⩽2%). The minute strain zone is taken so that the configuration ensures linear elastic destruction and obeys Hooke's law. The calculated elastic modulus at different temperatures is presented in Figure 4e. Analogous to the fracture strain and strength, the calculated elastic modulus also shows decreasing behavior with increasing temperature. As revealed in Figure 4e, when the temperature increases from 300 to 1000 K, the elastic moduli decline from ∼388.7 to ∼358.3 GPa with a ∼7.82% lessening and from ∼377.99 to ∼349.44 GPa with a ∼7.55% reduction along the armchair and zigzag directions, respectively. This happens because, at an increased temperature, Si−Si, Si−Ge, and Ge−Ge bonds suffer more significant thermal vibration and achieve superior mobility, which increases the mean distance between the atoms. Our attained results of elastic modulus of pristine 2D-SiGe are on a similar order of extent to those of MoS_2 and graphene oxide. At room temperature, the perfect MoS_2 sheet provides an elastic modulus of ∼(260−400) GPa,[48,49] whereas for armchair- and zigzag-oriented 2D-SiGe, they were 388.7 and 377.99 GPa, respectively.

To quantitatively expose the effect of temperature on the fracture behavior, the deformation process of 2D-SiGe is also explored via the stress-distribution profile at 1000 K (shown in Figure 5a−h). Combining the results of Figure 3a−h and Figure 5a−h, we found that the critical strain at which the sheet shows a breakdown is significantly reduced when the temperature is increased from 300 to 1000 K. At high temperatures, the early void creation and consequent failure happen at almost a similar strain level, which recommends a brittle failure mechanism. More importantly, due to the high temperature-induced thermal effect, the fracture of zigzag SiGe bonds occurs at an early strain. The nearby broken bonds would distract the process of phase transformation and accumulate into outsized defects at the edge, leading to the united fracture at a strain of about 28.2%. Therefore, there is no chance to go to the significant deformation strain needed for SLED at higher temperatures, and the zigzag-oriented 2D-SiGe shows a normal stress−strain behavior similar to other 2D materials.[41,50] Figure 5a−h and their zoomed in view can clearly describe the effect of temperature on the stress−strain behavior compared to 300 K. The zigzag-oriented sheet shows a nearly hexagonal structure when the temperature is increased

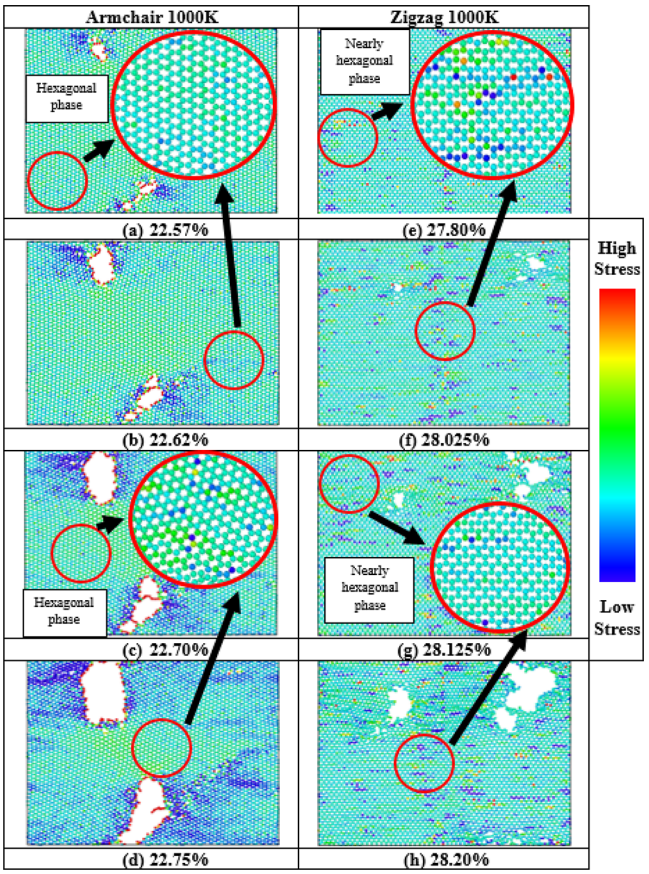

Figure 5. Sheet rupturing profile of 2D-SiGe along the (a−d) armchair and (e−h) zigzag orientations at 1000 K.

to 1000 K, and the irregular arrangement of the atoms is also reduced at this stage.

We analyzed the radial distribution function (RDF) of 2D-SiGe at two different temperatures to better understand the temperature effect. The influences from Si−Ge, Si−Si, and Ge−Ge pairs to RDFs are shown in Figure 6a−c, respectively. In general, for a monolayer structure,[39] the RDF can be specified as $g_{PQ}(r) = \frac{\Delta n_{PQ}}{2\pi r \Delta r \rho_Q}$, where $g_{PQ}(r)$ is the RDF, ρ_Q is the average density of atoms Q in the entire material, and Δn_{PQ} is the average number of atoms of type Q existing in the annular area between r and $r + \Delta r$ with a P atom at the center. At 0 K temperature, the RDF should be a delta function. When the temperature increases, the atoms start vibrating from their equilibrium site. Consequently, the possibility of finding a specific atom in the vicinity of the reference atom decreases with increasing temperature. Thus, with increasing temperature, the calculated RDFs for all the neighbors show a broadening of the delta functions, and the intensity of the peaks show softening nature. This behavior of the RDF peaks is related to the improved oscillations of atoms at higher temperatures and verifies the weak mechanical strength of 2D-SiGe.[51] From Figure 6a−c, it is also probed that the peak positions of the first, second, and third neighbors of the 2D-SiGe sheet correspond to 2.375, 4.045, and 4.105 Å, respectively, and indicate the validity of our RDF calculation for 2D-SiGe.

The fabrication of pristine nanomaterials is almost impossible. Various structural defects induced during synthesis can have unanticipated effects on the mechanical character-

https://doi.org/10.1021/acsomega.1c01691
ACS Omega 2021, 6, 21861−21871

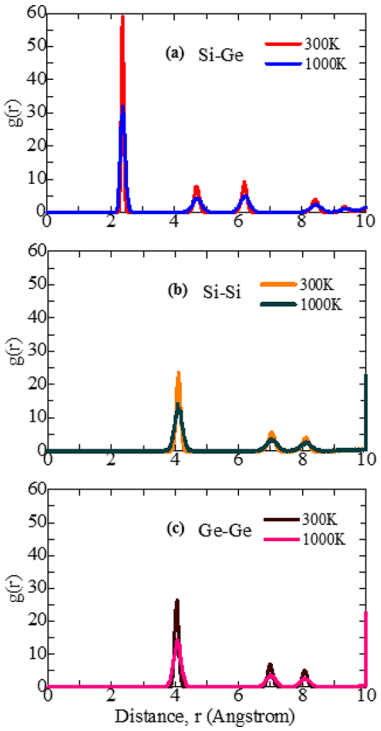

Figure 6. Radial distribution function, $g(r)$, of (a) Si−Ge, (b) Si−Si, and (c) Ge−Ge pairs in a SiGe sheet at two different temperatures.

istics of nanostructured materials. In addition, defects may also be a suitable way to govern the electronic and mechanical performances of 2D-SiGe. In MD simulation, the density of vacancy defects, interstitials defects, and their motion through the lattice can be easily identified by Wigner-Seitz (WS) defect analysis techniques.[36,52] In the WS method, to determine the defect density, two types of configurations are used. One is reference configuration (defect-free structure), and another is displaced configuration (vacancy-induced system). By comparing the displaced configuration with the reference configuration, the density of vacancy or interstitial defects can be easily identified. In addition, using MD simulation, the potential energy per atom calculation is an excellent tool that can characterize the types of defects, defect concentration, and temperature variation of a nanostructure.[41,53−55] Generally, when the structure is pristine at zero strain, the potential energy per atom shows a significantly lower energy value. However, the initial potential energy per atom would offer a larger value when the structure is defective. We have calculated the potential energy per atom of 2D-SiGe considering pristine, 1% BV, and 1% PV defects to identify the impact of defects and their types. The calculated potential energy per atom is shown in Figure 7a,b. During tensile loading, the potential energy per atom of 2D-SiGe increases monotonically. However, at the critical strain, when some of the covalent bonds of the structure break, the potential energy per atom shows a sudden drop and beyond which the simulations are terminated. Moreover, for both orientations, the pristine structure possesses a lower initial potential energy per atom than the vacancy-induced system. Additionally, among the two different vacancies considered in this study, the PV-induced structure shows a higher initial potential energy per atom than the BV-induced system due to its more significant symmetry breakdown effect at the same concentration.

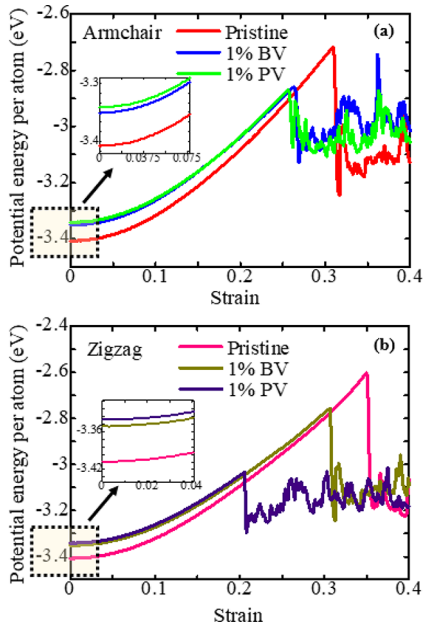

Figure 7. Calculated potential energy per atom as a function of the uniaxial strain of pristine and vacancy-induced 2D-SiGe along the (a) armchair and (b) zigzag orientations. The zoomed in view shows the variation of the energy value of 2D-SiGe under pristine and vacancy conditions.

To evaluate the probability of defect (vacancy) formation and characterize the thermodynamic stability of vacancy defects, we have also calculated the formation energies of PV and BV defects in 2D-SiGe. The vacancy formation energy E_v^f in the unit of eV is calculated using the following formula:[31]

$$E_v^f = E_f - [(N_0 - N_v)/N_0] \times E_i \quad (4)$$

where E_i denotes the initial energy of the pristine 2D-SiGe structure and E_f denotes the final energy of the vacancy-induced 2D-SiGe. N_0 represents the total number of atoms in 2D-SiGe before incorporating vacancy, and N_v represents the total number of atoms removed from the pristine 2D-SiGe structure. Table 1 shows the calculated values of formation energies of PV and BV defects of 2D-SiGe along with previously calculated DFT[56] and MD[57] simulations. Our calculation revealed that the formation energy of PV defect (Si or Ge) is lower than that of BV defect. Therefore, the probabilities of forming PV defect are higher compared to BV defect in 2D-SiGe. The vacancy formation energies obtained in our study also correspond well with the DFT and MD calculations.

Table 1. Formation Energies for PV and BV Defects in 2D-SiGe[a]

vacancy type	present study	DFT[56]	MD[57]
PV(Si)	3.361 ± 0.023	2.55	3.3957
PV(Ge)	3.345 ± 0.017	3.10	3.2769
BV	4.151 ± 0.107	3.40	4.4348−4.4353

[a]The margin of error is provided for five different simulation samples.

In this section, we have explored the point and bi vacancy-induced mechanical behaviors of 2D-SiGe. Figures 8a,b and 9a,b present the stress−strain relationship of point and bi vacancy-defected sheet with vacancy concentrations of 1.0−

https://doi.org/10.1021/acsomega.1c01691
ACS Omega 2021, 6, 21861−21871

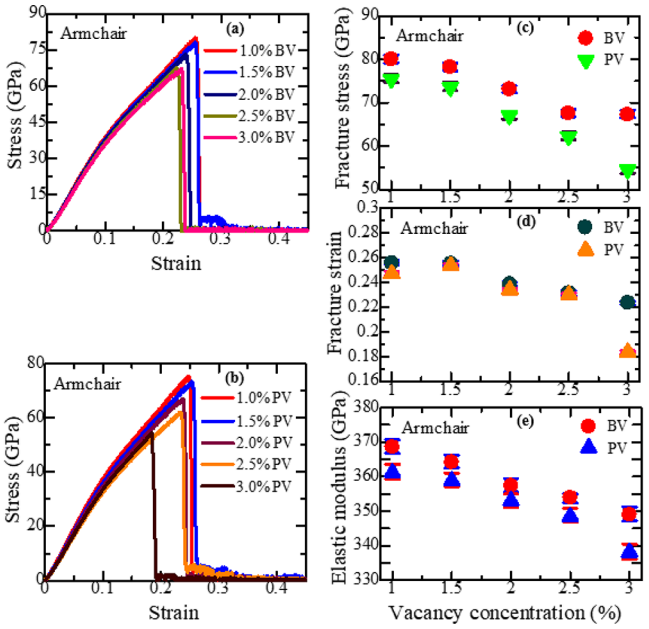

Figure 8. Stress−strain relationship of (a) bi and (b) point vacancy-defected 2D-SiGe at 300 K along the armchair orientation. Vacancy-induced (c) fracture strength, (d) fracture strain, and (e) elastic modulus of 2D-SiGe along the armchair orientation.

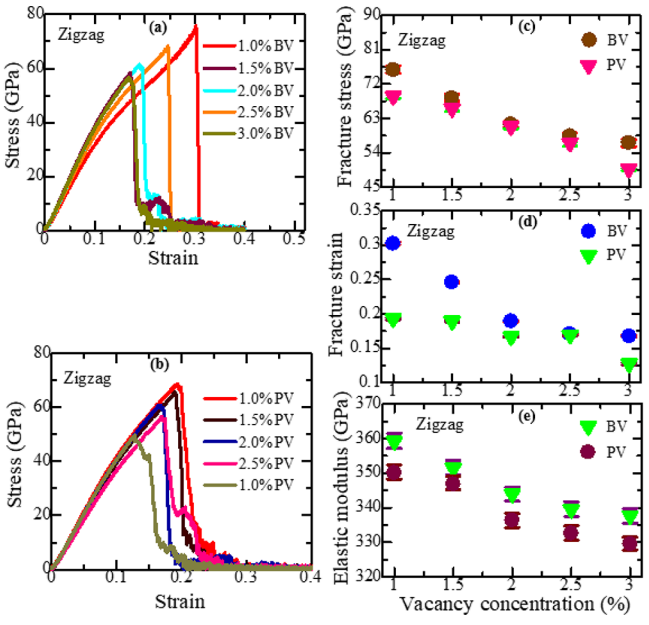

Figure 9. Stress−strain relationship of (a) bi and (b) point vacancy-defected 2D-SiGe at 300 K along the zigzag orientation. Vacancy-induced (c) fracture strength, (d) fracture strain, and (e) elastic modulus of 2D-SiGe along the zigzag orientation.

3.0% at 300 K in the armchair and zigzag orientations, respectively. For the pristine case, the calculated fracture strength, elastic modulus, and fracture strain along the armchair orientation are reported as ∼94.83, ∼388.7, and ∼0.3127, respectively, whereas these values are calculated as ∼91.92 GPa, ∼377.99 GPa, and ∼0.3604, respectively, for the zigzag orientation. The changes in fracture properties with different vacancy concentrations are displayed in Figures 8c,d and 9c,d. As Figures 8c,d and 9c,d illustrate, with the increase in vacancy concentration, both the fracture strength and strain decline monotonically. For a 1.0% BV in the armchair orientation, the fracture strength is diminished to ∼80.01 GPa, whereas for a 1.0% PV, the fracture strength is found as ∼75.41 GPa. Moreover, in the zigzag orientation, 2D-SiGe exhibits fracture strengths of ∼75.73 and ∼68.86 GPa, respectively, for 1.0% BV and PV. Moreover, the decrease in elastic modulus with vacancy concentration for both armchair and zigzag orientations is depicted in Figures 8e and 9e, respectively. It is perceived that the lessening of elastic modulus is more significant in PV defect. For a 1% PV, the elastic moduli have declined to ∼7.08 and ∼7.38% in the armchair and zigzag direction, respectively, which are nearly 1.4−1.5 times more significant than the lessening of BV-induced 2D-SiGe at room temperature. Jing et al.[58] and Islam et al.[22] also provided comparable results of elastic modulus of graphene and 2D-SiC with bi and point vacancy defects. The effects of BV and PV concentration on the percentage decrease of different mechanical properties of 2D-SiGe in the armchair and zigzag orientation are presented in Tables 2 and 3 separately. For all vacancy concentrations, the stress−strain response of 2D-SiGe displays a brittle fracture-like pristine nanosheet and is comparable to the finding of other 2D nanosheets.[59,60]

The stress distribution and deformation progression via bond breaking for BV and PV, respectively, have been demonstrated in Figure 10a−d and Figure 10e−h. The figures suggest that defective SiGe sheets face substantial stress concentration at the vacancy area even at a relatively lesser strain. A hole expanded from the vacancy site during tension. The failure then extends near the vacancy, awaiting the complete destruction of the damaged sheets. It should be noted that the closer these defects were to the boundaries, the greater the mechanical loads perpendicular to the loading direction were and the greater the stress concentration was in these areas. In bi vacancy- and point vacancy-induced 2D-SiGe, the development of early voids, the enlargement of these voids, and the ultimate cracking of the samples also show the analogous fashion of the pristine 2D-SiGe. As illustrated in Figure 10, the rupture begins from the vacancy position, and the path of crack promulgation is along the upright trend of the bi and point vacancy defects. In vacancy-defected 2D-SiGe, the early de-bonding endorses further de-bonding of silicon and germanium atoms, which further causes a huge number of single atomic chains of silicon and germanium atoms and hence leads to structure breaking. Unlike pristine 2D-SiGe, in the circumstance of BV and PV defects, the destruction of the sample is further limited, and the rest of the 2D-SiGe sheet remains very nearly unaffected. In addition, for both types of vacancies, with increasing defect concentrations, the critical strain needed to crack the sheet is also diminished and the vacancy-induced zigzag stress−strain relationship shows a normal behavior. This usual trend of the vacancy-induced zigzag stress−strain curve comes from the fact that when vacancy defect is incorporated into the pristine sheet, there is no chance to go to the large deformation strain region responsible for phase transformation as well as SLED, and therefore, the zigzag-oriented 2D-SiGe shows a normal stress−strain behavior.

In practical uses, the employed loading variation can considerably influence the mechanical behavior of the used nanomaterials. Especially during the variation of strain rates, a substantial alteration in the fracture performances has occurred. Here, as mentioned earlier, a strain rate of 1 ×

https://doi.org/10.1021/acsomega.1c01691
ACS Omega 2021, 6, 21861−21871

Table 2. Effects of Bi Vacancy and Point Vacancy Concentration on the Percentage Decrease of Different Mechanical Properties of 2D-SiGe along the Armchair Direction

	bi vacancy			point vacancy		
vacancy concentration (%)	fracture strength (%)	fracture strain (%)	elastic modulus (%)	fracture strength (%)	fracture strain (%)	elastic modulus (%)
1.0	15.63	18.19	5.17	20.47	21.01	7.08
1.5	17.55	18.35	6.29	22.44	18.89	7.69
2.0	22.89	23.63	8.05	29.33	25.17	9.19
2.5	28.76	25.96	8.94	34.43	26.45	10.35
3.0	29.08	28.49	10.20	42.53	41.32	13.01

Table 3. Effects of Bi Vacancy and Point Vacancy Concentration on the Percentage Decrease of Different Mechanical Properties of 2D-SiGe along the Zigzag Direction

	bi vacancy			point vacancy		
vacancy concentration (%)	fracture strength (%)	fracture strain (%)	elastic modulus (%)	fracture strength (%)	fracture strain (%)	elastic modulus (%)
1.0	17.61	16.09	4.95	25.08	46.42	7.38
1.5	25.58	31.74	7.01	28.57	47.39	8.24
2.0	33.10	47.42	8.98	33.68	53.60	37.47
2.5	36.44	52.58	10.17	38.41	52.99	12.01
3.0	38.39	53.49	10.65	45.77	64.53	12.82

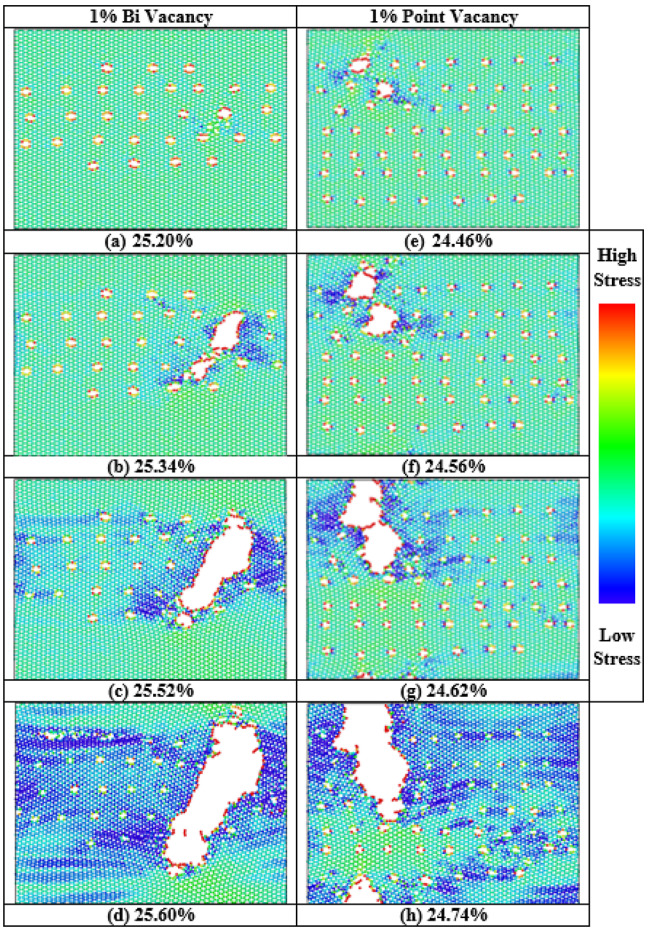

Figure 10. (a−d) Bi and (e−h) point vacancy-induced fracture spreading profiles at 300 K.

10^{-3} ps^{-1} and the effect of additional strain rates such as 5×10^{-4} and 5×10^{-5} ps^{-1} are also explored. The explored strain−stress relationships for armchair- and zigzag-directed 2D-SiGe at various strain rates are shown in Figure 11a,b. An identical temperature of 300 K is applied in all circumstances. The elastic regions of the strain−stress plots are extremely

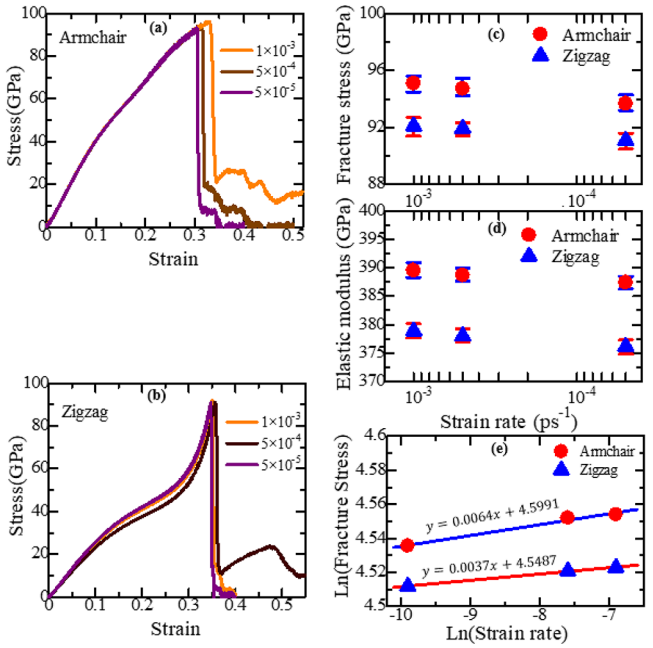

Figure 11. Effects of different strain rates on the strain−stress relationship of (a) armchair- and (b) zigzag-directed 2D-SiGe. Strain rate-based (c) fracture strength and (d) elastic modulus of 2D-SiGe along the two chiral directions. (e) Strain rate sensitivity along the two chiral directions.

coincided, demonstrating the insensitivity of elastic modulus to the strain rate in 2D-SiGe. The fracture strength and the corresponding elastic modulus for both types of chiralities reveal minor growing tendencies with increasing strain rates, as shown in Figure 11c,d. Of late, several works have been implemented on diverse nanomaterials, including *h*-BN, graphynes, and $MoSe_2$ with various strain rates.[37,46,61] These works also discover that the strain rate has a very slight influence on the fracture behavior on the nanoscale materials. To evaluate the sensitivity of fracture strength to the strain rate, here we have applied the Arrhenius formula, which can be expressed as[61]

https://doi.org/10.1021/acsomega.1c01691
ACS Omega 2021, 6, 21861−21871

$$\dot{\varepsilon} = A\sigma^{1/m}\exp\left(-\frac{Q}{RT}\right) \quad (5)$$

where $\dot{\varepsilon}$ denotes the strain rate, σ denotes the tensile strength, Q represents the activation energy, R denotes the universal gas constant, T denotes the deformation temperature, m denotes the strain rate sensitivity, and A means a constant. Equation 5 can be further shortened by receiving logarithms on both parts and adopting the fact that the system temperature is stable throughout the distortion. Hence, we can get

$$\ln \dot{\varepsilon} = \ln(A) + \frac{1}{m}\ln(\sigma) - \frac{Q}{RT} \quad (6)$$

Currently, by computing the slopes of $\ln(\sigma)$ and $\ln(\dot{\varepsilon})$ terms, the strain rate sensitivity m can be attained simply. The strain rate sensitivity m is stated as

$$m = \frac{\partial \ln(\sigma)}{\partial \ln(\dot{\varepsilon})} \quad (7)$$

The obtained strain rate sensitivity feature is shown in Figure 11e. It can be perceived that the strain rate sensitivity m values of 2D-SiGe in the armchair and zigzag orientations are 0.0064 and 0.0037, respectively. This is because, in pristine SiGe, two bonds in a unit cell are parallel to the armchair loading direction. However, in the case of the zigzag direction, there are no bonds that are parallel to the loading direction. Therefore, the sensitivity of 2D-SiGe along the armchair orientation is slightly larger than that along the zigzag orientation, signifying that the strain rate has a strong impact on the armchair-oriented mechanical properties of 2D-SiGe.

Finally, the size effect has also been explored to ensure that the 2D-SiGe structure used in this work (~408.9 nm^2) is large enough to generate size-independent results. For this purpose, two additional SiGe sheets of areas ~102.2 and ~920.1 nm^2 are taken. The explored fracture strength, strain, and elastic modulus of 2D-SiGe with the considered sheet areas are illustrated in Figure S1 (Supporting Information). As we have applied periodic boundary conditions in all three directions, the obtained mechanical properties of 2D-SiGe are also size-independent as expected.

CONCLUSIONS

In conclusion, the impact of temperature, chirality, and vacancy defects on the uniaxial tensile mechanical behavior of 2D-SiGe has been systematically explored through MD simulation. The stress−strain relationship exhibits a brittle style fracture for all concentrations of the vacancy on SiGe. Ultimate fracture strength along the armchair orientation is noticed to be larger than that along the zigzag orientation, which is an exciting spectacle for 2D honeycomb configurations. Higher temperature diminishes fracture strength and strain, and these declines are more substantial in the case of zigzag loading. It is explored that as the temperature increases, the softening and broadening of RDF peaks increase. Furthermore, among the two vacancies, a more significant reduction of the mechanical strength for both armchair and zigzag orientation is found for point vacancy defects owing to their more substantial symmetry breakdown effect. Our MD investigation suggests that only 1% PV decreases fracture strengths and strains by 20.47 and 21.01%, respectively, for armchair orientation as well as 25.08% and 46.42% for zigzag orientation. The deformation process of 2D-SiGe is also explored via the stress distribution profile at the different strain levels. It is shown that near the fracture strain, the armchair structures do not show any phase variation, and the hexagonal lattice structure is conserved for the whole system. However, along the zigzag direction, due to the phase transformation, the hexagonal lattice structure is converted into a quasi-rectangular lattice and an unphysical stress−strain relationship is found for this chirality. For both chiralities, initial voids are restricted to an insignificant zone, and the regions around the void of the structure stay unspoiled. The dependencies of elastic modulus, fracture strength, and fracture strain on strain rates and sheet areas reveal that the fracture properties of 2D-SiGe are less sensitive to the variations of strain rates and areas compared to temperatures and vacancy defects. This investigation would offer an exhaustive perception of the uniaxial mechanical and fracture propagation behavior of 2D-SiGe, which would further adapt the design of SiGe-based NEMS and nanoelectronics where defects are unavoidable.

ASSOCIATED CONTENT

Supporting Information

The Supporting Information is available free of charge at https://pubs.acs.org/doi/10.1021/acsomega.1c01691.

Effect of sheet areas on the stress−strain behavior of 2D-SiGe along the armchair and zigzag directions and sheet area-dependent fracture strength, fracture strain, and elastic modulus of 2D-SiGe along the two chiral directions (PDF)

AUTHOR INFORMATION

Corresponding Author

Md. Sherajul Islam − *Department of Electrical and Electronic Engineering, Khulna University of Engineering & Technology, Khulna 9203, Bangladesh; Department of Electrical and Biomedical Engineering, University of Nevada, Reno, Nevada 89557, United States;* orcid.org/0000-0002-6717-2523; Email: sheraj_kuet@eee.kuet.ac.bd

Authors

A. S. M. Jannatul Islam − *Department of Electrical and Electronic Engineering, Khulna University of Engineering & Technology, Khulna 9203, Bangladesh;* orcid.org/0000-0003-2101-6223

Md. Shahadat Akbar − *Department of Electrical and Electronic Engineering, Khulna University of Engineering & Technology, Khulna 9203, Bangladesh;* orcid.org/0000-0001-6920-0981

Jeongwon Park − *School of Electrical Engineering and Computer Science, University of Ottawa, Ottawa, ON K1N 6N5, Canada; Department of Electrical and Biomedical Engineering, University of Nevada, Reno, Nevada 89557, United States*

Complete contact information is available at: https://pubs.acs.org/10.1021/acsomega.1c01691

Author Contributions

A.S.M.J.I. contributed in conceptualization, methodology, software, and writing (original draft preparation). M.S.A. contributed in software, data curation, and writing (original draft preparation). M.S.I. contributed in visualization, investigation, writing (reviewing and editing). J.P. supervised the study and contributed in writing (reviewing and editing).

Notes

The authors declare no competing financial interest.

■ ACKNOWLEDGMENTS

This study was supported by the facilities of the UGC funded research project (grant no. CASR-55/23, 2020-2021), provided by the CASR at Khulna University of Engineering & Technology, Bangladesh.

■ REFERENCES

(1) Manzeli, S.; Dumcenco, D.; Migliato Marega, G.; Kis, A. Self-Sensing, Tunable Monolayer MoS2 Nanoelectromechanical Resonators. *Nat. Commun.* **2019**, *10*, 4831−4837.
(2) Qian, Z.; Liu, F.; Hui, Y.; Kar, S.; Rinaldi, M. Graphene as a Massless Electrode for Ultrahigh-Frequency Piezoelectric Nanoelectromechanical Systems. *Nano Lett.* **2015**, *15*, 4599−4604.
(3) Androulidakis, C.; Zhang, K.; Robertson, M.; Tawfick, S. Tailoring the Mechanical Properties of 2D Mater. and Heterostructures. *2D Mater.* **2018**, *5*, No. 032005. IOP Publishing Ltd June
(4) Kuperman, M.; Nagar, L.; Peskin, U. Mechanical Stabilization of Nanoscale Conductors by Plasmon Oscillations. *Nano Lett.* **2020**, *20*, 5531−5537.
(5) Islam, M. S.; Ushida, K.; Tanaka, S.; Makino, T.; Hashimoto, A. Effect of Boron and Nitrogen Doping with Native Point Defects on the Vibrational Properties of Graphene. *Comput. Mater. Sci.* **2014**, *94*, 35−43.
(6) Rashid, A. S.; Islam, M. S.; Ferdous, N.; Anindya, K. N.; Park, J.; Hashimoto, A. Widely Tunable Electronic Properties in Graphene/Two-Dimensional Silicon Carbide van Der Waals Heterostructures. *J. Comput. Electron.* **2019**, *18*, 836−845.
(7) Chen, Y.; Xiao, H.; Liu, Y.; Chen, X. Effects of Temperature and Strain Rate on Mechanical Behaviors of Stone-Wales Defective Monolayer Black Phosphorene. *J. Phys. Chem. C* **2018**, *122*, 6368−6378.
(8) Islam, M. S.; Tamakawa, D.; Tanaka, S.; Makino, T.; Hashimoto, A. Polarized Microscopic Laser Raman Scattering Spectroscopy for Edge Structure of Epitaxial Graphene and Localized Vibrational Mode. *Carbon* **2014**, *77*, 1073−1081.
(9) Novoselov, K. S.; Fal'Ko, V. I.; Colombo, L.; Gellert, P. R.; Schwab, M. G.; Kim, K. A. Roadmap for Graphene. *Nature* **2012**, *490*, 192−200.
(10) Guilhon, I.; Teles, L. K.; Marques, M.; Pela, R. R.; Bechstedt, F. Influence of Structure and Thermodynamic Stability on Electronic Properties of Two-Dimensional SiC, SiGe, and GeC Alloys. *Phys. Rev. B* **2015**, *92*, No. 075435.
(11) Şahin, H.; Cahangirov, S.; Topsakal, M.; Bekaroglu, E.; Akturk, E.; Senger, R. T.; Ciraci, S. Monolayer Honeycomb Structures of Group-IV Elements and III-V Binary Compounds: First-Principles Calculations. *Phys. Rev. B* **2009**, *80*, 155453.
(12) Lee, K. W.; Lee, C. E. Strain-Induced Topological Phase Transition with Inversion of the in-Plane Electric Polarization in Tiny-Gap Semiconductor SiGe Monolayer. *Sci. Rep.* **2020**, *10*, 11300.
(13) Zhou, H.; Zhao, M.; Zhang, X.; Dong, W.; Wang, X.; Bu, H.; Wang, A. First-Principles Prediction of a New Dirac-Fermion Material: Silicon Germanide Monolayer. *J. Phys. Condens. Matter* **2013**, *25*, 395501.
(14) Jamdagni, P.; Kumar, A.; Thakur, A.; Pandey, R.; Ahluwalia, P. K. Stability and Electronic Properties of SiGe-Based 2D Layered Structures. *Mater. Res. Express* **2015**, *2*, No. 016301.
(15) Mohebpour, M. A.; Mozvashi, S. M.; Vishkayi, S. I.; Tagani, M. B. Prediction of Hydrogenated Group IV−V Hexagonal Binary Monolayers. *Sci. Rep.* **2020**, *10*, 14963.
(16) Sannyal, A.; Ahn, Y.; Jang, J. First-Principles Study on the Two-Dimensional Siligene (2D SiGe)as an Anode Material of an Alkali Metal Ion Battery. *Comput. Mater. Sci.* **2019**, *165*, 121−128.
(17) Choi, S. M.; Jhi, S. H.; Son, Y. W. Effects of Strain on Electronic Properties of Graphene. *Phys. Rev. B* **2010**, *81*, No. 081407.
(18) Yan, J. A.; Gao, S. P.; Stein, R.; Coard, G. Tuning the Electronic Structure of Silicene and Germanene by Biaxial Strain and Electric Field. *Phys. Rev. B* **2015**, *91*, 245403.
(19) Sakib, H.; Ahmed, T.; Subrina, S. Uniaxial Strain on Monolayer SiGe: Strain Tunable Electronic Properties. In *2018 10th International Conference on Electrical and Computer Engineering (ICECE)*; IEEE: *2018*; pp. 313−316, DOI: 10.1109/ICECE.2018.8636776.
(20) Behzad, S. Effect of Uni-Axial and Bi-Axial Strains and Vertical Electric Field on Free Standing Buckled Germanene. *J. Electron Spectros. Relat. Phenom.* **2018**, *229*, 13−19.
(21) Zhao, H.; Aluru, N. R. Temperature and Strain-Rate Dependent Fracture Strength of Graphene. *J. Appl. Phys.* **2010**, *108*, No. 064321.
(22) Islam, A. S. M. J.; Islam, M. S.; Ferdous, N.; Park, J.; Bhuiyan, A. G.; Hashimoto, A. Anisotropic Mechanical Behavior of Two Dimensional Silicon Carbide: Effect of Temperature and Vacancy Defects. *Mater. Res. Express* **2019**, *6*, 125073.
(23) Sha, Z. D.; Pei, Q. X.; Ding, Z.; Jiang, J. W.; Zhang, Y. W. Mechanical Properties and Fracture Behavior of Single-Layer Phosphorene at Finite Temperatures. *J. Phys. D: Appl. Phys.* **2015**, *48*, 395303.
(24) Islam, A. S. M. J.; Islam, M. S.; Ferdous, N.; Park, J.; Hashimoto, A. Vacancy-Induced Thermal Transport in Two-Dimensional Silicon Carbide: A Reverse Non-Equilibrium Molecular Dynamics Study. *Phys. Chem. Chem. Phys.* **2020**, *22*, 13592−13602.
(25) Anindya, K. N.; Islam, M. S.; Hashimoto, A.; Park, J. Combined Effect of 13C Isotope and Vacancies on the Phonon Properties in AB Stacked Bilayer Graphene. *Carbon* **2020**, *168*, 22−31.
(26) Islam, M. S.; Tanaka, S.; Hashimoto, A. Effect of Vacancy Defects on Phonon Properties of Hydrogen Passivated Graphene Nanoribbons. *Carbon* **2014**, *80*, 146−154.
(27) Islam, M. S.; Ushida, K.; Tanaka, S.; Hashimoto, A. Numerical Experiments on Phonon Properties of Isotope and Vacancy-Type Disordered Graphene. *Diamond Relat. Mater.* **2013**, *40*, 115−122.
(28) Islam, M. S.; Ushida, K.; Tanaka, S.; Hashimoto, A. Numerical Analysis on Vacancy Induced Vibrational Properties of Graphene Nanoribbons. *Comput. Mater. Sci.* **2013**, *79*, 356−361.
(29) Mahata, A.; Jiang, J. W.; Mahapatra, D. R.; Rabczuk, T. Effect of Intrinsic Structural Defects on Mechanical Properties of Single Layer MoS 2. *Nano-Struct.s Nano-Objects* **2019**, *18*, 100247.
(30) Paul, R.; Tasnim, T.; Saha, S.; Motalab, M. Atomistic Analysis to Characterize the Impact of Temperature and Defects on the Mechanical Properties of Germanene Sheet. *Mater. Res. Express* **2018**, *5*, No. 015062.
(31) Das, S.; Mojumder, S.; Rakib, T.; Islam, M. M.; Motalab, M. Atomistic Insights into Mechanical and Thermal Properties of Stanene with Defects. *Phys. B* **2019**, *553*, 127−136.
(32) Ahammed, S.; Islam, M. S.; Mia, I.; Park, J. Lateral and Flexural Thermal Transport in Stanene/2D-SiC Van Der Waals Heterostructure. *Nanotechnology* **2020**, *31*, 505702.
(33) Sun, X.; Guo, Y.; Zhao, Y.; Liu, S.; Li, H. Gas Adsorption Investigation on SiGe Monolayer: A First-Principle Calculation. *Sensors* **2020**, *20*, 2879.
(34) Plimpton, S. Fast Parallel Algorithms for Short-Range Molecular Dynamics. *J. Comput. Phys.* **1995**, *117*, 1−19.
(35) Tersoff, J. Modeling Solid-State Chemistry: Interatomic Potentials for Multicomponent Systems. *Phys. Rev. B* **1989**, *39*, 5566−5568.
(36) Stukowski, A. Visualization and Analysis of Atomistic Simulation Data with OVITO-the Open Visualization Tool. *Modell. Simul. Mater. Sci. Eng.* **2010**, *18*, No. 015012.
(37) Zhang, Y. Y.; Pei, Q. X.; Mai, Y. W.; Gu, Y. T. Temperature and Strain-Rate Dependent Fracture Strength of Graphynes. *J. Phys. D: Appl. Phys.* **2014**, *47*, 425301.
(38) Tsai, D. H. The Virial Theorem and Stress Calculation in Molecular Dynamics. *J. Chem. Phys.* **1979**, *70*, 1375−1382.
(39) Thomas, S.; Ajith, K. M.; Valsakumar, M. C. Empirical Potential Influence and Effect of Temperature on the Mechanical

Properties of Pristine and Defective Hexagonal Boron Nitride. *Mater. Res. Express* **2017**, *4*, No. 065005.
(40) Zhang, Y. Y.; Pei, Q. X.; Sha, Z. D.; Zhang, Y. W. A Molecular Dynamics Study of the Mechanical Properties of H-BCN Monolayer Using a Modified Tersoff Interatomic Potential. *Phys. Lett. A* **2019**, *383*, 2821−2827.
(41) Sun, Y. J.; Huang, Y. H.; Ma, F.; Ma, D. Y.; Hu, T. W.; Xu, K. W. Molecular Dynamics Simulation on Double-Elastic Deformation of Zigzag Graphene Nanoribbons at Low Temperature. *Mater. Sci. Eng. B* **2014**, *180*, 1−6.
(42) Thomas, S.; Lee, S. U. Atomistic Insights into the Anisotropic Mechanical Properties and Role of Ripples on the Thermal Expansion of H-BCN Monolayers. *RSC Adv.* **2019**, *9*, 1238−1246.
(43) Mortazavi, B.; Madjet, M. E.; Shahrokhi, M.; Ahzi, S.; Zhuang, X.; Rabczuk, T. Nanoporous Graphene: A 2D Semiconductor with Anisotropic Mechanical, Optical and Thermal Conduction Properties. *Carbon* **2019**, *147*, 377−384.
(44) Mortazavi, B. Ultra High Stiffness and Thermal Conductivity of Graphene like C3N. *Carbon* **2017**, *118*, 25−34.
(45) Mortazavi, B.; Ahzi, S. Thermal Conductivity and Tensile Response of Defective Graphene: A Molecular Dynamics Study. *Carbon* **2013**, *63*, 460−470.
(46) Li, N.; Ding, N.; Qu, S.; Liu, L.; Guo, W.; Wu, C. M. L. Mechanical Properties and Failure Behavior of Hexagonal Boron Nitride Sheets with Nano-Cracks. *Comput. Mater. Sci.* **2017**, *140*, 356−366.
(47) Islam, A. S. M. J.; Islam, M. S.; Ferdous, N.; Park, J.; Bhuiyan, A. G.; Hashimoto, A. Anomalous Temperature Dependent Thermal Conductivity of Two-Dimensional Silicon Carbide. *Nanotechnology* **2019**, *30*, 445707.
(48) Wang, X.; Han, D.; Hong, Y.; Sun, H.; Zhang, J.; Zhang, J. Machine Learning Enabled Prediction of Mechanical Properties of Tungsten Disulfide Monolayer. *ACS Omega* **2019**, *4*, 10121−10128.
(49) Castellanos-Gomez, A.; Poot, M.; Steele, G. A.; van der Zant, H. S. J.; Agraït, N.; Rubio-Bollinger, G. Elastic Properties of Freely Suspended MoS_2 Nanosheets. *Adv. Mater.* **2012**, *24*, 772−775.
(50) Yang, Z.; Huang, Y.; Ma, F.; Sun, Y.; Xu, K.; Chu, P. K. Temperature and Strain-Rate Effects on the Deformation Behaviors of Nano-Crystalline Graphene Sheets. *Eur. Phys. J. B* **2015**, *88*, 1−8.
(51) Thomas, S.; Ajith, K. M.; Chandra, S.; Valsakumar, M. C. Temperature Dependent Structural Properties and Bending Rigidity of Pristine and Defective Hexagonal Boron Nitride. *J. Phys. Condens. Matter* **2015**, *27*, 315302.
(52) Ji, L.; Liu, L.; Xu, Z.; Song, Y.; Jin, T.; Li, R.; Fang, F. Molecular Dynamics Simulation on the Effect of Dislocation Structures on the Retention and Distribution of Helium Ions Implanted into Silicon. *Nanotechnol. Precis. Eng.* **2020**, *3*, 81−87.
(53) Lu, Q.; Gao, W.; Huang, R. Atomistic Simulation and Continuum Modeling of Graphene Nanoribbons under Uniaxial Tension. *Modell. Simul. Mater. Sci. Eng.* **2011**, *19*, No. 054006.
(54) Shi, J.; Hu, C.; Shen, J.; Cai, K.; Wang, J. Mechanical Properties of Bonded Few-Layered Graphene via Uniaxial Test: A Molecular Dynamics Simulation Study. *Comput. Mater. Sci.* **2020**, *172*, 109295.
(55) Budarapu, P. R.; Javvaji, B.; Sutrakar, V. K.; Mahapatra, D. R.; Paggi, M.; Zi, G.; Rabczuk, T. Lattice Orientation and Crack Size Effect on the Mechanical Properties of Graphene. *Int. J. Fract.* **2017**, *203*, 81−98.
(56) Shen, L.; Zhang, X.; Lu, J.; Wang, J.; Li, C.; Xiang, G. The Effect of Vacancy Defects on the Conductive Properties of SiGe. *Phys. Lett. A* **2021**, *386*, 126993.
(57) Sadki, K.; Zanane, F. Z.; Ouahman, M.; Drissi, L. B. Molecular Dynamics Study of Pristine and Defective Hexagonal BN, SiC and SiGe Monolayers. *Mater. Chem. Phys.* **2020**, *242*, 122474.
(58) Jing, N.; Xue, Q.; Ling, C.; Shan, M.; Zhang, T.; Zhou, X.; Jiao, Z. Effect of Defects on Young's Modulus of Graphene Sheets: A Molecular Dynamics Simulation. *RSC Adv.* **2012**, *2*, 9124−9129.
(59) Mortazavi, B.; Rémond, Y. Investigation of Tensile Response and Thermal Conductivity of Boron-Nitride Nanosheets Using Molecular Dynamics Simulations. *Phys. E* **2012**, *44*, 1846−1852.
(60) Yin, H.; Qi, H. J.; Fan, F.; Zhu, T.; Wang, B.; Wei, Y. Griffith Criterion for Brittle Fracture in Graphene. *Nano Lett.* **2015**, *15*, 1918−1924.
(61) Wang, X.; Hong, Y.; Wang, M.; Xin, G.; Yue, Y.; Zhang, J. Mechanical Properties of Molybdenum Diselenide Revealed by Molecular Dynamics Simulation and Support Vector Machine. *Phys. Chem. Chem. Phys.* **2019**, *21*, 9159−9167.

https://doi.org/10.1021/acsomega.1c01691
ACS Omega 2021, 6, 21861−21871